MONITORING FOREST ECOSYSTEM VEGETATION CHANGES BY COMBINING NDVCI INDEX ANALYSIS AND REMOTE SENSING TECHNOLOGY

CHEN, W. X.[1,2*] – GUO, H. X.[3] – SHIN, A. L. M.[1] – LI, R.[2]

[1]*Faculty of Built Environment and Surveying, Universiti Teknologi Malaysia, Johor 81310, Malaysia*

[2]*School of History Geography and Tourism, Chengdu Normal University, Sichuan 611130, China*

[3]*School of Chemistry and Life Science, Chengdu Normal University, Sichuan 611130, China*

**Corresponding author*
e-mail: chenwenxi85@163.com

(Received 21st May 2025; accepted 31st Jul 2025)

Abstract. To more accurately monitor changes in forest vegetation, the study combines the normalized difference vegetation index with remote sensing technology. The study proposes using multi-source remote sensing images and detection algorithms to automatically monitor changes in forest vegetation. First, remote sensing image data were obtained from GF-1 and Landsat8 satellites, and then preprocessed through calibration and other methods to obtain clear remote sensing image maps. Then, the dynamic change characteristics of remote sensing images were analyzed. Based on this, a threshold classification algorithm based on normalized difference vegetation change index was constructed. Finally, an empirical analysis was conducted using the Sanjiangyuan region as an example. The results indicated that the vegetation coverage rate in the Sanjiangyuan area was mainly low in 2018, at about 32%. The vegetation coverage rate in 2022 was mainly medium coverage and high coverage, which were about 30% and 31% respectively. In addition, it is known that cultivated and forested land in the Sanjiangyuan area is gradually increasing, while grassland and other types of vegetation are decreasing. The results indicate that the method used in this study can achieve automatic monitoring of forest vegetation changes.
Keywords: *forest resources, normalized difference vegetation change index, satellite remote sensing data, vegetation cover, environmental resources*

Introduction

As one of the Earth's most significant ecosystems, forests play a vital role in preserving the Earth's ecological balance and protecting human habitats due their biodiversity, vegetation cover, and ecological functions (Abd El-Ghany et al., 2020). However, with the acceleration of industrialization and the increase of anthropogenic activities, FEs (forest ecosystems, FEs) are facing many challenges, such as indiscriminate logging, frequent fires, and the spread of pests and diseases, which have a serious impact on the stability and health status of FE (Cuaran and Leon, 2021; Virnodkar et al., 2020). Therefore, reliable and efficient VC (vegetation change, VC) monitoring in FE has emerged as a key area for future study. To study the change pattern of Rhantarium epapposum vegetation in Abdali Reserve, Al-Ali et al. (2020) constructed a detection system by using UAV multispectral imagery, examining vegetation indices and categorization methods. The findings indicated that the altered vegetation index performed better than the normalized vegetation index in dry shrubs and grasslands. Additionally, it was discovered that the maximum likelihood classifier and support vector machine outperformed the others, with a kappa coefficient of 0.89 and an overall accuracy

http://www.aloki.hu ● ISSN 1589 1623 (Print) ● ISSN 1785 0037 (Online)
DOI: http://dx.doi.org/10.15666/aeer/2305_92359253

of 93%. Kattenborn et al. (2021) proposed the application of CNNs (convolutional neural networks, CNNs) in vegetation RS (remote sensing, RS) in order to investigate the effectiveness of such techniques in vegetation identification and monitoring. A literature review was conducted to illustrate the application and effectiveness of CNNs on different problems. It was found that CNNs were effective in extracting spatial patterns from RSI (remote sensing image, RSI). Chenyu et al. (2022) proposed a method that utilized multi-temporal Landsat satellite images, combined object-oriented methods and random forest algorithms in order to study typical wetland VCs (vegetation changes, VCs) in the current Yellow River Mouth Nature Reserve. The method utilized RSID (remote sensing image data, RSID) and a specific algorithm to classify wetland vegetation and analyze its spatial and temporal change characteristics. According to the findings, the technique was capable of efficiently tracking how the marsh vegetation in the Yellow River Mouth Nature Reserve changed recently. To increase the sample size, Zhang and Shao employed LiDAR data to estimate the aboveground biomass of urban vegetation. According to the study's findings, categorization could increase the inversion accuracy of calculating the biomass of urban vegetation. To evaluate changes in land use and cover and their effects on surface temperature within a county, Hussain and Karuppannan (2023)employed RS methods. Using a maximum likelihood approach, a supervised classification technique was used to find LULC changes in the research area. The approach could monitor the target area's land use, according to the results. To analyze the changes in forest vegetation, Zeng et al. (2021) investigated the importance of vegetation indices and their application in vegetation dynamics. Reliability in drawing conclusions regarding changes in ecosystems was hampered by variations in various indices, sensors, quality control procedures, synthesis algorithms, and atmospheric and sun-target-sensor geometry corrections. It can be concluded that VC monitoring of FE using RS technology has become an important research direction. RS technology provides strong technical support for FE monitoring with its fast, wide range and real-time characteristics. Among them, NDVCI (normalized difference vegetation change index, NDVCI), as an important vegetation index, shows great potential in monitoring forest VC. Nevertheless, there are still significant issues with the current RS monitoring techniques based on NDVCI index, even though they may partially accomplish the monitoring of forest VC. First off, a thorough examination of the types of forest vegetation, their distribution patterns, and their interactions with other ecological factors is lacking in the majority of current techniques, which primarily concentrate on changes in the NDVCI index itself. Secondly, the accuracy of the monitoring results is also affected by the issue of precision and resolution of RS data. Moreover, there may be large differences in FE in different regions and time periods, which also poses a challenge to the universality and applicability of monitoring methods. This study aims to integrate RS approaches and NDVCI index analysis to address the inadequacies of current VC detection methods. This will enable a comprehensive and accurate monitoring model for forest VC to be developed. It is expected that it can provide more powerful support for DC (dynamic changes, DC) of vegetation, ecological environmental protection and sustainable development.

There are four sections to the study. The initial segment primarily examines the rationale behind investigating VC of FE and the present state of research, merging these two aspects to suggest the research approach and goal. The second section mainly describes the acquisition method of RS data in the target area, the preprocessing method and the specific construction of the VC monitoring algorithm. After outlining the experimental parameters in Section three, experiments are designed to confirm the

http://www.aloki.hu ● ISSN 1589 1623 (Print) ● ISSN 1785 0037 (Online)
DOI: http://dx.doi.org/10.15666/aeer/2305_92359253

suggested approach. In Section four, the experimental data are mostly summarized and analyzed, and the study's limitations are suggested.

One of the innovations of the study is to use various correction methods and IF (image fusion, IF) methods to preprocess the RSI to provide quality data for subsequent vegetation DC monitoring. The second is to construct a threshold classification algorithm based on NDVCI to improve the accuracy of vegetation DC monitoring in response to the shortcomings of existing VC index monitoring methods.

The study quantifies the dynamic changes of forest vegetation by constructing a classification algorithm based on the NDVCI threshold. Firstly, NDVCI is calculated using the red and near-infrared bands of GF-1 and Landsat 8. The multi-phase NDVCI grayscale mean μ and standard deviation σ are used as the classification threshold. When the NDVCI of a pixel exceeds $\mu \pm k\,\sigma$ ($k \in [0.1,2.0]$), it is considered that the vegetation has undergone an "increase" or "decrease" change; Subsequently, a multi-level similarity zone aggregation rule was established by combining spectral, texture, PSNR, and spatial features. Areas with NDVI > 0.8 were identified as vegetation and subdivided into forest land, farmland, grassland, and wetland. With NDVI as the core indicator, fine characterization of changes in forest vegetation coverage and types was achieved.

Methods and materials

Data collection and preprocessing methods

To accurately determine the VC of FE, the study uses GF-1 and Landsat8 satellites to acquire high-resolution multispectral and panchromatic infrared RSIDs. GF-1 satellite imagery uses PMS multispectral sensor data with a spatial resolution of 8 m. It includes blue, green, red, and near-infrared bands. The time range is the 2018-2022 growing season (June-September), and the cloud cover is less than 10%. Landsat 8 OLI images: Level-1T pre-processing products (spatial resolution 30 m) are selected, including visible light to shortwave infrared bands (with emphasis on Band 4 Red, Band 5 NIR, Band 6 SWIR1), synchronized with GF-1 in time. The 50 m resolution digital elevation model is used for terrain correction, while the administrative division vector boundary is used for image cropping. Moreover, for localized special areas, camera equipment carried by UAVs is used to acquire higher resolution image data to provide more detailed information (Cui et al., 2023; Xue et al., 2021). The collected RSIDs are usually affected by external factors such as different geographic environments, resulting in poor quality of RSI, which has a greater impact on the analysis and utilization of the data at a later stage (Liu et al., 2020). Therefore, preprocessing the RS data images obtained is required to increase the RSID visualization effect and the image evaluation accuracy. The specific steps are shown in *Figure 1*.

In *Figure 1*, sensor calibration converts the DN (digital number, DN) acquired by satellite sensors into the top-of-atmosphere radiant brightness with actual physical significance, thus eliminating the radiometric errors generated by the sensors themselves and ensuring the accuracy and reliability of the data. The quantitative relationship between DN and radiant brightness or reflectance is established through radiometric calibration. The study adopts the GF-1 image and Landsat8 image to calibrate the sensor, as shown in *Equation 1* (Zhong et al., 2020).

$$L(\lambda) = Gain * DN(\lambda) + Bias \quad \text{(Eq.1)}$$

http://www.aloki.hu ● ISSN 1589 1623 (Print) ● ISSN 1785 0037 (Online)
DOI: http://dx.doi.org/10.15666/aeer/2305_92359253

In *Equation 1*, $L(\lambda)$ is the radiant brightness value and $DN(\lambda)$ is the DN value for band λ. $Gain$ is the gain parameter and $Bias$ is the offset parameter.

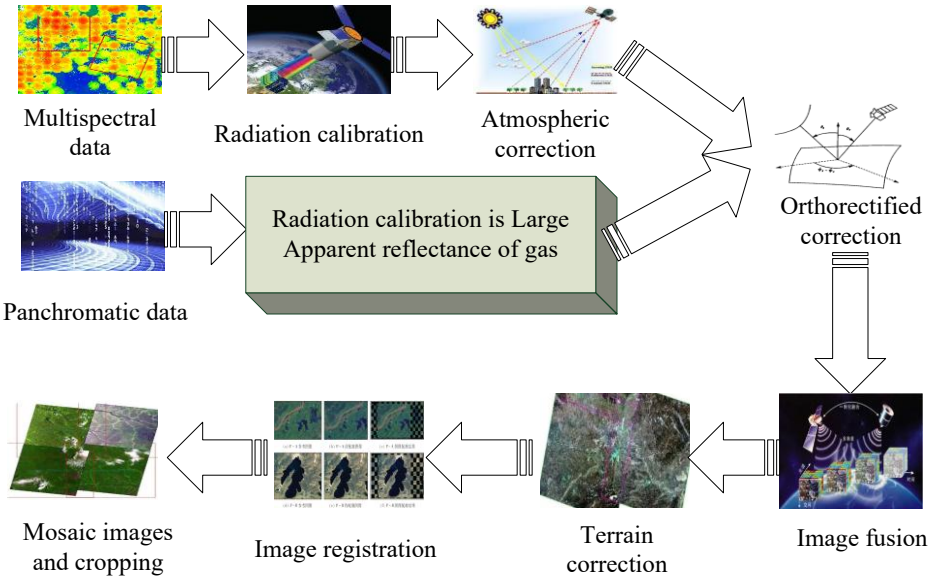

Figure 1. *RSID preprocessing flow*

Atmospheric correction can complete the quantization of RS information, and the study uses the FLAASH atmospheric correction function in ENVI software to correct the RSI image by image to obtain model parameters that are closer to the real radiative reflectivity of ground objects. In this process, the diffuse radiant energy is constant at a fixed angle of incidence, and the diffuse reflective surface in this state is called the Lambertian surface (Xie et al., 2021). The FLAASH atmospheric correction is based on the transport model of MODTRAN radiation. The model treats the ground as a Lambertian surface and uses this to establish *Equation 2* for the spectral irradiance of the image element.

$$L = \left(\frac{A * \rho}{1 - \rho_e * S}\right) + \left(\frac{B * \rho}{1 - \rho_e * S}\right) + L_a \quad \text{(Eq.2)}$$

In *Equation 2*, L is the total radiant brightness. ρ is the albedo of the entire Lambertian surface and ρ_e is the average surface albedo of the entire Lambertian surface. A and B are the coefficients, and L_a is the atmospheric backscattering radiance. The unknowns in the formula can be calculated from the image data collected by RS satellites combined with the MODTRAN model. The MODTRAN model is then used to invert the computed atmospheric parameters to complete the correction of the atmospheric data. Orthographic correction uses digital elevation model data to adjust the terrain deformation of each element in an RSI image. This ensures the image has the correct geographic coordinates and meets the conditions of an orthographic projection (Hu et al., 2020; Bhosle and Musande, 2023)). The study adopts the 50-m resolution digital elevation model data combined with the software's own correction function to orthorectify the RSID, which can reduce the impact of uneven terrain distribution in the RSI. For RSIF (remote sensing

http://www.aloki.hu ● ISSN 1589 1623 (Print) ● ISSN 1785 0037 (Online)
DOI: http://dx.doi.org/10.15666/aeer/2305_92359253

image fusion, RSIF), the study uses a two-branch attention network for fusion, and the specific structure is shown in *Figure 2*.

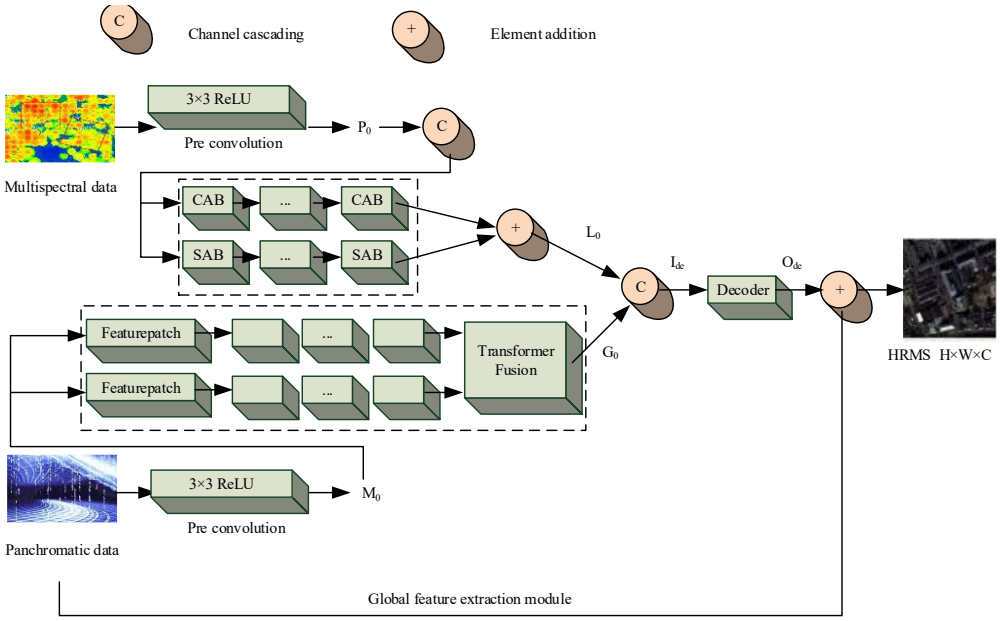

Figure 2. *Overall structure of remote sensing image fusion network*

As shown in *Figure 2*, the entire RSIF modeling equation is given in *Equation 3*.

$$HRMS = \lambda\left(\left[PAN, MS\right]\right) + MS \tag{Eq.3}$$

In *Equation 3*, $HRMS$ is the result of RSIF. MS is the experimental data after Gaussian blurring after upsampling of multispectral images. $\lambda(\bullet)$ is the network framework shown in *Figure 2*. The whole fusion process is based on the acquired RSI multispectral data and panchromatic data as input. The panchromatic and multispectral images are then feature mapped by two 3×3 convolution kernels to ensure that they enter the same feature space. After that, the feature maps are processed utilizing both a global and a local FEB (feature extraction branch, FEB). The image's local features are captured by the six separate convolutional modules that make up the local FEB. The multi-head convolutional attention mechanism of Transformer is employed by the global FEB to acquire knowledge of the image's spectral and spatial properties. The model then performs multilevel decoding of the fused features and introduces residual concatenation. This passes the original multispectral image information directly to the decoder's output, ultimately generating a high-resolution multispectral image.

The vegetation of FE is located in a variety of terrain transformations, terrain slope and terrain slope direction, etc. will affect the effect of the fused RSI, resulting in the phenomenon of image recognition error (Abba Haruna et al., 2022). In the study, the C correction method in the Lambertian body model is used to correct the terrain, as shown in *Equation 4* (Al-Hamzawi et al., 2021).

$$L_m = L * \frac{\cos\beta + c}{\cos i + c} \tag{Eq.4}$$

http://www.aloki.hu ● ISSN 1589 1623 (Print) ● ISSN 1785 0037 (Online)
DOI: http://dx.doi.org/10.15666/aeer/2305_92359253

In *Equation 4*, L and L_m are the pixel values before and after topographic correction, respectively. $\cos i$ and $\cos\beta$ are both cosine values of the solar incidence angle. c is the semi-empirical coefficient, as shown in *Equation 5*.

$$c = \frac{b}{k} \quad \text{(Eq.5)}$$

In *Equation 5*, b and k are the intercept and slope, respectively, in the statistical regression equation of the Lambertian body model. After topographic correction, further elimination of geometric positional bias among multi-scene RSIs is required. The study uses the automatic alignment function of ENVI software to process the alignment of the collected RSIs using the standard RSIs as benchmarks. Finally, the processed neighboring RSIs are spliced to form the required RSI study area for the study, and the area is irregularly cropped using vector boundary data to obtain the final RSI map.

Characterization of remote sensing image dynamic changes

After the preprocessing of RSI is completed, the change features of the target object, such as shape and color, can be identified and extracted from the RS satellite image (Paz-Alberto et al., 2021). Because the change features have different spectral characteristics, brightness value laws and possibly different texture information in the image from the unchanged image (He et al., 2022), the study selects spectral features, texture features, PSNR (peak signal-to-noise ratio, PSNR), and spatial features as the basis for the change of RSI information, as shown in *Figure 3*.

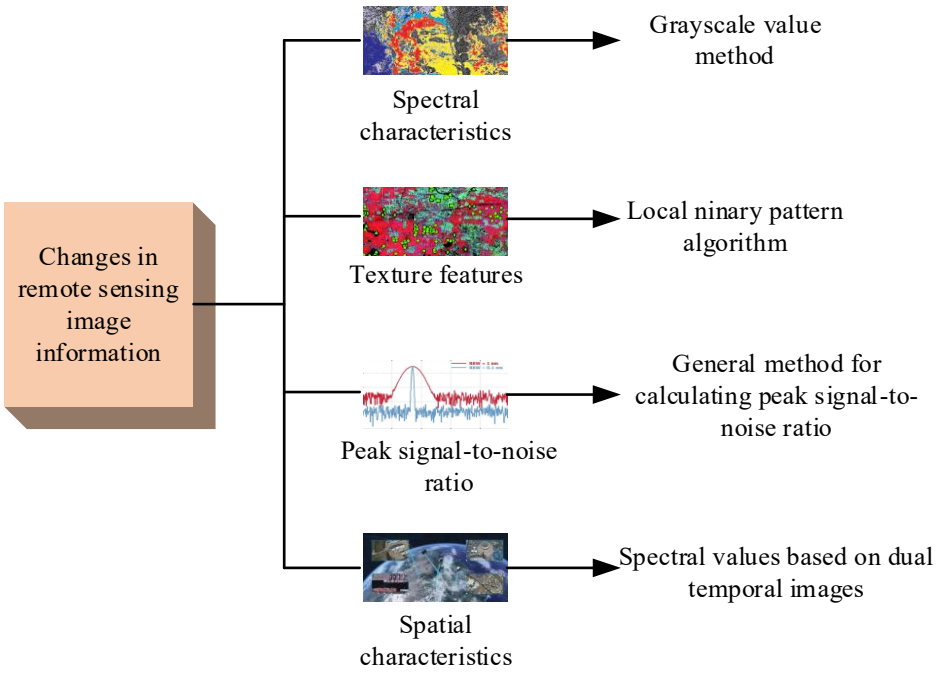

Figure 3. *Characterization method of remote sensing image dynamic changes*

As shown in *Figure 3*, for the variation of the spectral features, the study is carried out by calculating the average GV (gray value, GV) of all pixels in the superpixel block. The

http://www.aloki.hu ● ISSN 1589 1623 (Print) ● ISSN 1785 0037 (Online)
DOI: http://dx.doi.org/10.15666/aeer/2305_92359253

process is performed independently for each band of the multispectral image, so that a spectral feature value is obtained for each band. This processing is carried out with the hyperpixel block as the basic unit, which reduces the effect of noise and thus improves the accuracy of spectral feature extraction. The spectral feature variation is plotted in *Equation 6* (Li, 2021).

$$I(j)=\frac{1}{K}\sum_{K=1}^{B}\sum_{C=1}^{P}\left|I_C^K(T_1,j)-I_C^K(T_2,j)\right| \quad \text{(Eq.6)}$$

In *Equation 6, B* is the number of bands in the RS multispectral image. *j* is the hyperpixel. $I(j)$ is the spectral variation intensity value of *j*. *P* is the total number of pixels and $I_C^K(T_1)$ is the spectral value at moment T_1. For texture features, the study uses the LBP (local binary pattern, LBP) algorithm as an extraction scheme for texture features. This method takes each pixel point in the RSI and generates a binary value to characterize its local texture features by comparing it with the surrounding pixels (Min et al., 2020; Huang et al., 2022). The LBP operator is computed in a 3 × 3 square area. When comparing the CP (center pixel, CP) to its neighbors, points larger than or equal to the CP are denoted as 1, and points less than the CP are denoted as 0. The procedure is depicted in *Figure* 4 and involves converting these binary data to decimal numbers as the LBP value for that particular area.

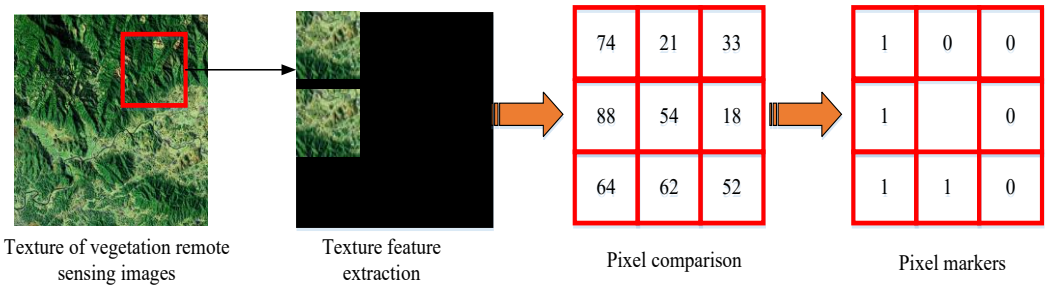

Figure 4. *Local binary pattern algorithm process*

The process is still analyzed in blocks of hyperpixels for each band. The intensity map of texture feature changes is shown in *Equation 7*.

$$F_L=\sqrt{\sum_{K=1}^{B}\left(L_{T_1}^K(j)-L_{T_2}^K(j)\right)^2} \quad \text{(Eq.7)}$$

In *Equation 7*, F_L is the texture feature variation intensity map. $L_{T_1}^K(j)$ is the LBP feature of the *K*th band for the *j*th superpixel. The mean square error *MSE* of the *j*th superpixel in the *K*th band of the RSI is shown in *Equation 8* (Lawrance and Angel, 2023).

$$MSE=\frac{1}{nK}\sum_{K=1}^{B}\sum_{i=1}^{P}\left(T_1(K,j,i)-T_2(K,j,i)\right)^2 \quad \text{(Eq.8)}$$

In *Equation 8*, $T_1(K,j,i)$ is the pixel value of RSI at the moment of T_1. The PSNR $F_P(j)$ is calculated according to *Equation 8*, as shown in *Equation 9*.

http://www.aloki.hu ● ISSN 1589 1623 (Print) ● ISSN 1785 0037 (Online)
DOI: http://dx.doi.org/10.15666/aeer/2305_92359253

$$F_P(j) = 10\log_{10}\left(\frac{MAX^2}{MSE}\right) \quad \text{(Eq.9)}$$

In *Equation 9*, *MAX* is the maximum value of the RSI pixel, which is set to 255. For the spatial features, it is based on the spectral values of the associated dual-temporal phase image. The study represents the magnitude and direction of the change in the dual time-phase spectra by the slope $F_{SL}(j)$ of the spatial feature as well as the intercept $F_I(j)$, as shown in *Equation 10* (Chen et al., 2022).

$$\begin{cases} F_{SL}(j) = \dfrac{B \times P \times S_{T_1T_2} - S_{T_1} \times S_{T_2}}{B \times P \times S_{T_1T_1} - S_{T_1} \times S_{T_1}} \\ F_I(j) = \dfrac{S_{T_2} - F_{SL} \times S_{T_1}}{B \times P} \end{cases} \quad \text{(Eq.10)}$$

In *Equation 10*, $S_{T_1T_2}$ is the product of the corresponding pixels of image T_1 and image T_2. S_{T_1} and S_{T_2} are the sum of the pixel values at moment T_1 and moment T_2, respectively.

Algorithm for detecting dynamic changes in vegetation based on the NDVCI index

The above studies have analyzed the characterization of RSI change detection, but it is not possible to accurately analyze the morphological change process of vegetation by relying only on RSI spectral features. Vegetation in FE can cause changes in RSI spectral properties during growth and development, which in turn affects the accuracy of vegetation identification and classification in RSI (Chi, 2021; Pan et al., 2021). Vegetation index can reflect the plant growth status through the combination of different bands on RSI, and the study uses a NDVCI threshold classification algorithm to analyze the plant growth status in the target area and to monitor the change of vegetation cover. The algorithm process is shown in *Figure 5*.

As shown in *Figure 5*, the algorithm is divided into four steps. The first step is to determine the VC index map, which is a step to select the RSI at different time points and calculate the VC index by comparing and analyzing the vegetation cover at these two time points, which is represented in the form of a grayscale image. After obtaining the VC index map, it is categorized using the threshold method. The threshold method classifies the vegetation in the image into different vegetation types such as grassland, crop land, forest land, etc. by setting a certain range of values. Then the similar regions in the classified images are further aggregated and analyzed for accuracy. When the accuracy verification results show that the classification accuracy meets the actual production requirements, the classification map can be used as the final VC classification map (Yang et al., 2020). In practice, the study uses the red and near-infrared bands of the GF-1 RSI and the red and mid-infrared bands of the Landsat8 RSI are used to capture changes in the vegetation surface over time. Differences in the data of these bands are used to identify the DC of the vegetation through temporal contrast (i.e., band differencing), thus effectively distinguishing between changed and unchanged vegetation areas. The NDVCI of the GF-1 RSI is shown in *Equation 11*.

$$NDVCI_{GF-1} = \left(\frac{NIR_{t1} - R_{t2}}{NIR_{t1} + R_{t2}}\right) - \left(\frac{NIR_{t2} - R_{t1}}{NIR_{t2} + R_{t1}}\right) \quad \text{(Eq.11)}$$

http://www.aloki.hu ● ISSN 1589 1623 (Print) ● ISSN 1785 0037 (Online)
DOI: http://dx.doi.org/10.15666/aeer/2305_92359253

In *Equation 11*, NIR and R are the 4th and 3rd bands of the GF-1 RSI, respectively. R_{t1} and R_{t2} are the red light bands of the pre and post periods, respectively. NIR_{t1} and NIR_{t2} are the near-infrared bands for the before and after periods, respectively. The NDVCI of Landsat8 RSI is shown in *Equation 12*.

$$NDVCI_{Landsat8} = \left(\frac{MIR_{t1} - R_{t2}}{MIR_{t1} + R_{t2}}\right) - \left(\frac{MIR_{t2} - R_{t1}}{MIR_{t2} + R_{t1}}\right) \quad \text{(Eq.12)}$$

In *Equation 12*, MIR and R are bands 6 and 4 of the Landsat8 RSI, respectively. The classification threshold T is to set the gray scale mean value of NDVCI as $\bar{m}$ and the standard deviation as ∂. When the classification threshold of NDVCI exceeds the set maximum or minimum value, it is considered that the image element of the corresponding RSI has changed. The classification threshold T is shown in *Equation 13* (Zhang et al., 2020).

$$T = \bar{m} + n\partial \quad \text{(Eq.13)}$$

In *Equation 13*, the empirical value of n is set to [0.1,2.0]. Substituting the interval spacing of the empirical values into *Equation 13*, the area of increase in vegetation is obtained as shown in *Equation 14* (Xu et al., 2020).

$$\begin{cases} (NDVI_1 > 0) \cup (NDVI_2 > 0) \\ NDVCI > T_{\max} \end{cases} \quad \text{(Eq.14)}$$

The areas of reduction in vegetation are shown in *Equation 15*.

$$\begin{cases} (NDVI_1 > 0) \cup (NDVI_2 > 0) \\ NDVCI < T_{\min} \end{cases} \quad \text{(Eq.15)}$$

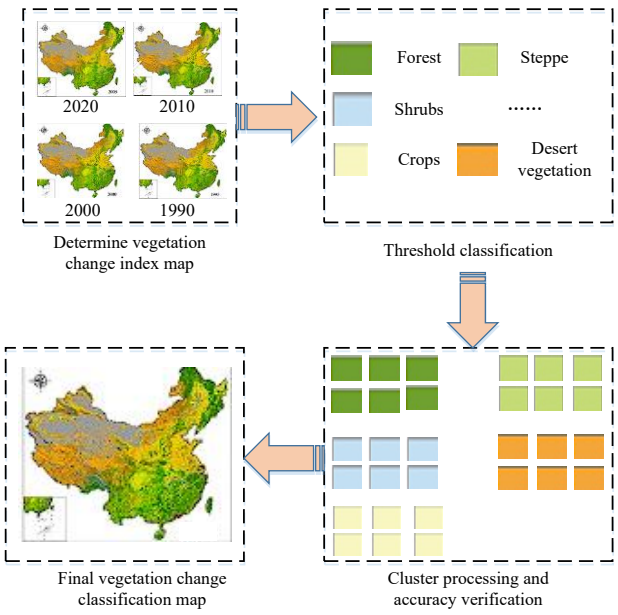

Figure 5. *Steps of NDVCI-based threshold classification algorithm*

http://www.aloki.hu ● ISSN 1589 1623 (Print) ● ISSN 1785 0037 (Online)
DOI: http://dx.doi.org/10.15666/aeer/2305_92359253

The classification map of VCs in FEs can be extracted based on the increasing and decreasing areas of vegetation. However, the VC classification map extracted in this way contains many trivial pixel patterns and can only distinguish between "VC" and "unchanged", or between simple coverage levels, such as "high", "medium", or "low." It is unable to accurately separate specific vegetation types, such as farmland, grassland, and wetlands. To achieve fine separation of different vegetation types (e.g., cultivated land, grassland, forest land, and wetlands) in FEs, a multi-level similar area aggregation method is introduced. This method is based on the coverage level map obtained by NDVCI threshold classification. The specific steps are shown in *Figure 6*.

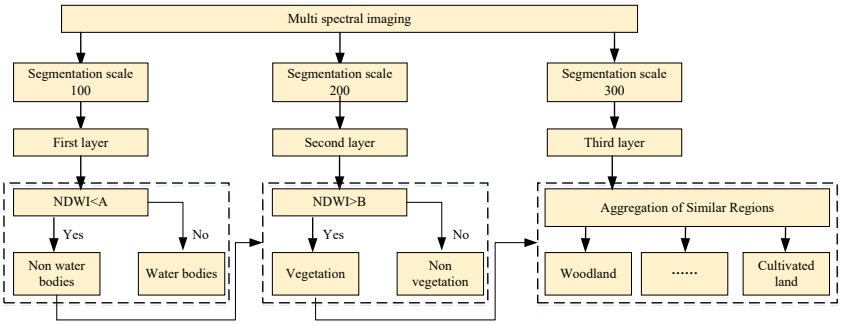

Figure 6. *Approach to multi-level similar region aggregation*

As shown in *Figure 6*, when the NDVCI value is less than the set 0.1 value, the terrain is identified as a water body. Otherwise, it is a non water body. When the NDVCI value is greater than the set value of 0.8, the terrain is identified as vegetation. Otherwise, it is non vegetation. Then, based on spectral features, texture features, peak signal-to-noise ratio, spatial features, and other information changes, vegetation is aggregated and classified to distinguish cultivated land, grassland, wetland, and forest land. The multi feature collaborative fine classification criteria are shown in *Table 1*.

Table 1. *Multi feature collaborative fine classification standards*

Type	Spectral characteristic range (Δ S)	Texture feature range (LBP variance Δ L)	Peak signal-to-noise ratio range (Δ G)	Spatial features (β)
Cultivated land	$\Delta S > 25$	$\Delta L > 8$	$\Delta G < 28$	$\beta > 0.3$
Grass	$10 < \Delta S < 20$	$\Delta L < 4$	$28 < \Delta G < 32$	$\beta < -0.2$
Nunja	$\Delta S < 10$	$5 < \Delta L < 7$	$\Delta G > 32.5$	$-0.2 < \beta < 0.2$
Woodland	$10 < \Delta S < 15$	$\Delta L > 2.5$	$\Delta G > 30$	$\beta > 0.2$

Table 1 shows the classification criteria used to distinguish and aggregate different types of terrain in FEs. Finally, after removing trivial pixel patches, the VC classification map of FEs can be obtained.

Results

Overview of the experimental area and setting of the experimental environment

To verify the effectiveness of the proposed method for VC monitoring of FE, the Sanjiangyuan area is selected as the experimental subject for the study. The latitude and

http://www.aloki.hu ● ISSN 1589 1623 (Print) ● ISSN 1785 0037 (Online)
DOI: http://dx.doi.org/10.15666/aeer/2305_92359253

longitude coordinates of the Sanjiangyuan area are roughly 31°39'-36°16'N and 89°24'-102°23'E, which belongs to the plateau cold semi-arid climate zone. The overall terrain in the region is high and steep, with an average elevation of more than 600 m above sea level (Jiang and Liu., 2024). Due to its location on a plateau, the region has a cold and dry climate, with low annual precipitation, which is mainly concentrated in the summer months, averaging about 400-500 mm per year. Its average annual temperature is below freezing, the winter is long and cold, and the summer is short and cool (Zhang et al., 2022). The long hours of sunshine and strong solar radiation throughout the year provide unique conditions for the unique ecological environment of the plateau. The northwestern part of the Sanjiangyuan area is mainly highland meadows and wetlands with good vegetation cover, and is an important water source for the Yangtze and Yellow Rivers. Its southeastern part, on the other hand, is mostly exposed rocks and a small amount of alpine meadows, with relatively light soil erosion. In response to the unique geographic profile of this region, the study selects the RSI collected by GF-1 and Landsat8 satellites from 2018-2022 as the basic data for the experiment.

Vegetation with different coverage is graded according to the number of pixels detected on the RSI. Vegetation cover (VCov) > 75% corresponds to "high cover". 75% > cover > 60% corresponds to "higher cover". 60% > coverage > 45% corresponds to a rating of "medium coverage". 45% > Coverage > 10% corresponds to "lower coverage". 10% > coverage corresponds to a rating of "low coverage".

Analysis of preprocessing effect of remote sensing image

Evaluation of remote sensing image correction effects

The study collects the 4th band of GF-1 RSI and the 6th band of Landsat8 RSI in the Sanjiangyuan area as experimental data, and the scenes mainly contain vegetation types such as cropland, grassland, and woodland. To compare with the correction methods used in the study, the wavelet threshold method and standard rectangle matching method are selected to process a series of corrections such as radiometric correction and geometric correction on the selected RSIs. The column mean distribution of RSI is shown in *Figure 7*.

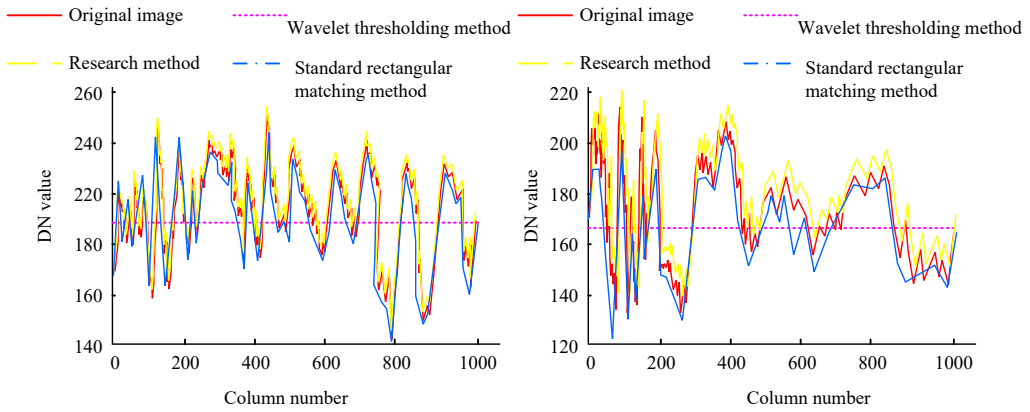

Figure 7. *Column mean distribution of remote sensing image*

In *Figure 7*, the mean GV of the OI (original image, OI) is in DC, but the mean GV of the standard rectangle matching method is unchanged. The data show that the standard

http://www.aloki.hu ● ISSN 1589 1623 (Print) ● ISSN 1785 0037 (Online)
DOI: http://dx.doi.org/10.15666/aeer/2305_92359253

rectangle matching method has a good denoising effect, which can remove most of the strip noise. However, from this result, the standard rectangle matching method changes the original gray scale distribution of the image, which will lose most of the details of the RSI and affect the subsequent results. The mean GV of image columns obtained using the wavelet thresholding method is consistent with OI fluctuations. However, the difference between the two is large enough that processing the RSI will result in some blurring and loss of detail. In contrast, the distribution of the mean GV of the image using the correction method in the study has a better overlap with the mean GV curve of the OI, with a degree of overlap of more than 99%, and eliminates the sharp peaks and valleys on the mean GV curve of the OI. More accurate brightness information can be obtained after such processing to ensure the completeness and accuracy of the image.

Remote sensing image fusion effect evaluation

For RSIF, the study adopts a two-branch attention network for IF. In order to objectively evaluate the fusion effect of this method, the study selects QI (quality index, QI), ORE (overall relative error, ORE), SAM (spectral angle, SAM), SCC (spatial correlation coefficient, SCC) four metrics to measure the fusion results of RSI low resolution. Spectral distortion index Dβ, spatial distortion index Dx, and reference-free QI QNR are used to measure the fusion results of RSI full resolution. The QI measures the similarity of brightness, contrast, and structure between the fused and reference images on a scale from 0 to 1. The closer it is to 1, the higher the fusion quality. ORE reflects the overall deviation between the fused image and the reference image, with smaller values indicating higher spectral fidelity. SAM evaluates the degree of spectral feature distortion, with smaller values indicating smaller spectral distortion. The spatial structure correlation between the fused SCC images and the reference images is determined using the Pearson correlation coefficient, which ranges from 0 to 1. The closer it is to 1, the better the preservation of spatial details. D β quantifies the spectral differences between fused and low-resolution multispectral images. Smaller values indicate better spectral consistency. Dx evaluates the differences in spatial detail between fused and high-resolution panchromatic images. Smaller values indicate more sufficient spatial information injection. QNR is a reference free metric that combines spectral and spatial distortion, with a closer value to 1 indicating better overall fusion quality. Moreover, the current popular fusion networks are selected as reference: MSDCNN (multi-scale dense CNN, MSDCNN), BDCNN (branch dense CNN, BDCNN), DICNN (dual independent CNN, DICNN), FNN (fusion neural network, FNN), DPNN (deep residual pyramid neural network, DPNN). The results are shown in *Table 2*.

In *Table 2*, both in the GF-1 RSI and in the Landsat8 RSI, the method used in the study has the highest QI and the smallest ORE in the images. Moreover, it is in good agreement with the reference image both in spectral signal, information and spatial structure.

Remote sensing image mosaicing and cropping effect evaluation

The assessment of RSI mosaicing and cropping effects is an important step in ensuring the quality and accuracy of the study data. By comparing the images before and after processing, the mood of the mosaiced images and the accuracy of cropping can be assessed. GF-1 RSI and Landsat8 RSI are selected for the study to test the clarity of the images of different vegetation types mosaiced and cropped by the research method, and the results are shown in *Figure 8*.

http://www.aloki.hu ● ISSN 1589 1623 (Print) ● ISSN 1785 0037 (Online)
DOI: http://dx.doi.org/10.15666/aeer/2305_92359253

Table 2. *Quantitative evaluation of fused images by different methods*

The 4th band of GF-1 remote sensing image							
Index	QI	ORE	SAM	SCC	Dβ	Dx	QNR
MSDCNN	0.899	1.689	2.489	0.941	0.041	0.121	0.857
BDCNN	0.835	2.321	3.247	0.912	0.101	0.195	0.732
FNN	0.921	1.634	2.342	0.964	0.107	0.035	0.865
DPNN	0.917	1.524	2.641	0.942	0.049	0.098	0.960
Research method	0.923	1.421	1.965	0.956	0.024	0.071	0.905
The 6th band of Landsat 8 remote sensing images							
Index	QI	ORE	SAM	SCC	Dβ	Dx	QNR
MSDCNN	0.954	3.236	5.142	0.951	0.032	0.054	0.985
BDCNN	0.942	3.684	6.352	0.945	0.031	0.102	0.862
FNN	0.965	3.214	4.652	0.955	0.063	0.022	0.896
DPNN	0.924	3.321	4.632	0.943	0.032	0.012	0.832
Research method	0.968	3.056	4.658	0.963	0.023	0.074	0.096

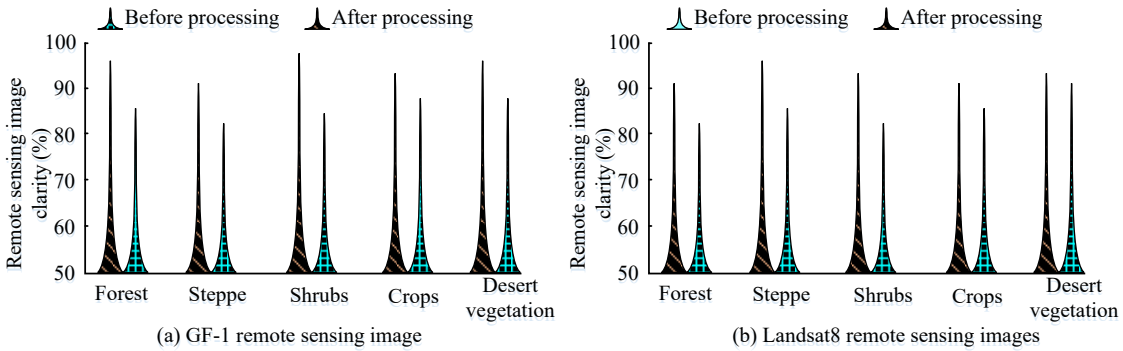

Figure 8. *Comparison of image sharpness before and after processing*

As shown in *Figure 8*, both GF-1 RSI and Landsat8 RSI obtain a certain improvement in image clarity after mosaicing and cropping by the research method. Before processing, the clarity of different vegetation types RS types is around 85%. Moreover, after the processing, the image clarity are above 90%. On the whole, the preprocessing of RSI effectively improves the overall image quality and provides a more reliable data base for the subsequent analysis of vegetation RS in FE.

Empirical analysis of vegetation changes in forest ecosystems in the Sanjiangyuan area

The study examines the situation of vegetation cover changes in the FE of the Sanjiangyuan area through the comparison of multi-period RSI, and the vegetation cover is expressed by NDVCI. According to the NDVCI formula provided by the study, ENVI software is used to calculate the VCov in June 7th, 2018, June 7th, 2020, June 7th, 2021 in the Sanjiangyuan area, and Google Earth Pro software is used to obtain the VCov of the region, as shown in *Figure 9*.

Figure 9a shows the variation of VCov in the Sanjiangyuan area calculated on the basis of GF-1 RSID, and *Figure 9b* shows the variation of VCov in the Sanjiangyuan area calculated on the basis of Landsat8 RSID. It can be concluded that the vegetation in the

http://www.aloki.hu ● ISSN 1589 1623 (Print) ● ISSN 1785 0037 (Online)
DOI: http://dx.doi.org/10.15666/aeer/2305_92359253

western and northern parts of the Sanjiangyuan area is sparse, with lower coverage. The vegetation in the central part of the area is more normal, with medium coverage. Moreover, the vegetation in the east is lush and high coverage. Moreover, from 2018 to 2020, with the passage of time, both the VCov reflected by GF-1 and Landsat8 RSID showed a general upward trend. The specific changes are shown in *Figure 10*.

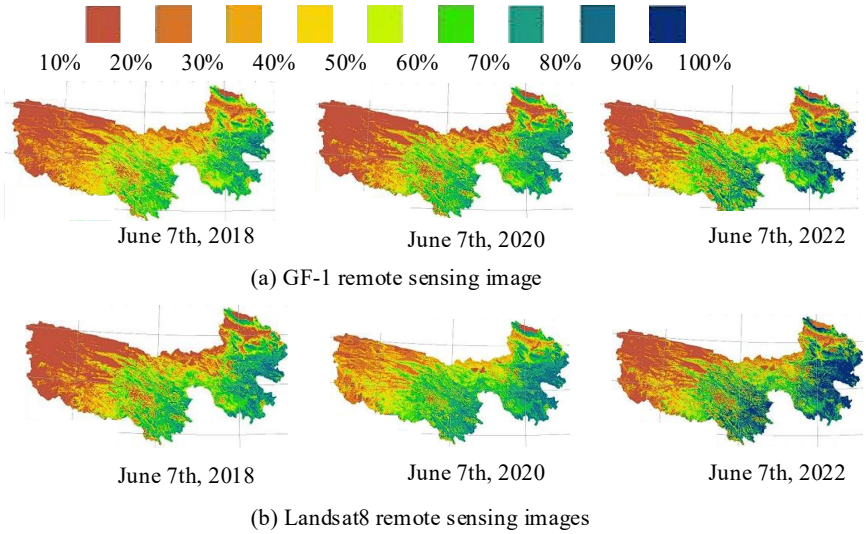

Figure 9. *Changes in vegetation cover in the Sanjiangyuan area*

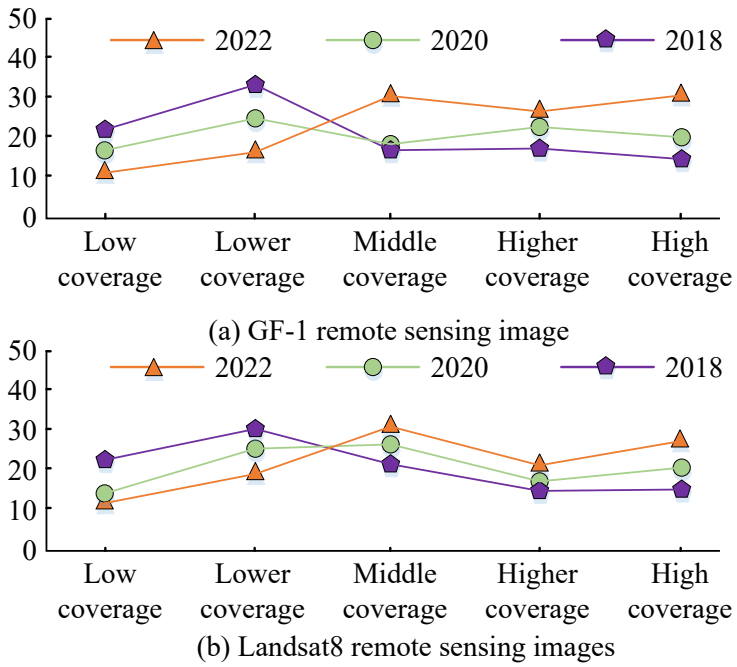

Figure 10. *Changes in the proportion of vegetation at various levels in the Sanjiangyuan area*

As shown in *Figure 10*, vegetation coverage in the Sanjiangyuan area is primarily low in 2018, at around 32%. The vegetation coverage in 2022 is mainly dominated by medium coverage and high coverage, which are about 30% and 31% respectively. This indicates

http://www.aloki.hu ● ISSN 1589 1623 (Print) ● ISSN 1785 0037 (Online)
DOI: http://dx.doi.org/10.15666/aeer/2305_92359253

that the research method can detect the VCov of the target area in real time, providing accurate, timely data. These data clearly indicate the trend of VCov in the Sanjiangyuan region, thus providing a better understanding of the ecological status of the region. This provides a scientific basis for ecological protection. To further study the details of VCov in the Sanjiangyuan area, the study uses the multilevel similar area aggregation's to categorize the vegetation in the Sanjiangyuan area into five types, such as forest land, cultivated land, grassland, wetland, and other. The classification accuracy of the method is examined with a confusion matrix, and the results are shown in *Figure 11*.

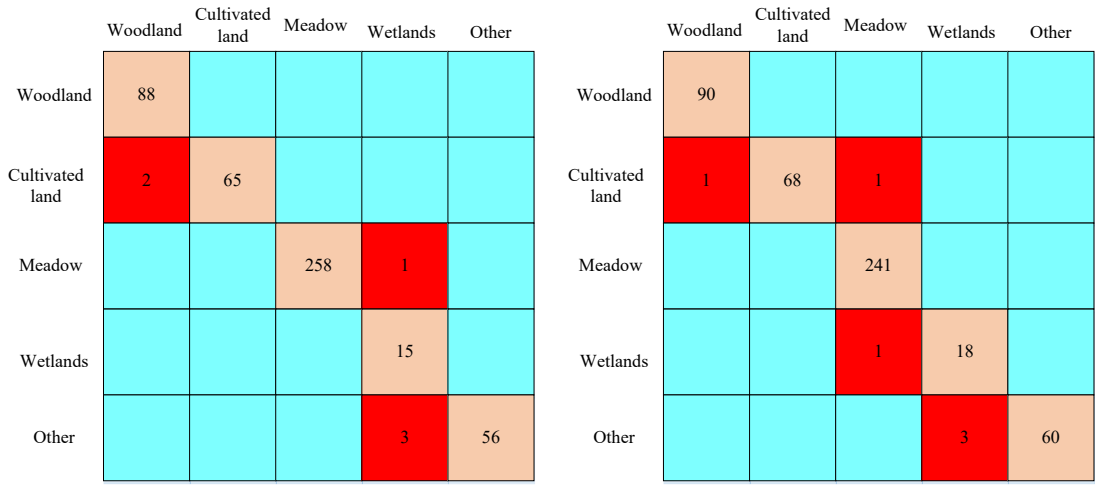

Figure 11. *Confusion matrix of vegetation multilevel similarity region clustering classification*

In *Figure 11*, the multilevel similar region aggregation classification method used in the study has a high accuracy in classifying vegetation types in the Sanjiangyuan area. In GF-1 RSID, only two forest land samples are misclassified as cropland, one grassland sample is misclassified as wetland, and three wetland samples are misclassified as other, with an overall classification accuracy of 98.6%. In Landsat8 RSID, there is 1 sample of cropland misclassified as woodland and grassland, respectively, and 3 samples of wetland misclassified as other, with an overall classification accuracy of 98.2%. To further demonstrate the superiority of the method, TSSPTC (the study selects pixel-based target classification, TSSPTC), DLTC (deep learning-based target classification, DLTC), and SSOTC (single-scale segmentation-oriented object target classification, SSOTC) are used to classify the RS dataset of the Sanjiangyuan area. *Figure 12* displays the classification accuracy findings.

In *Figure 12*, the classification method used in the study has the highest accuracy, above 98.2%, both in GF-1 RSID and Landsat8 RSID. This classification method aggregates similar regions at multiple levels, enabling it to more accurately capture and express the characteristics of different vegetation types in the RSI. This method fully satisfies the study's classification of vegetation types in the Sanjiangyuan area. On the other hand, target classification techniques based on pixels and deep learning have classification accuracy of roughly 92%. The single-scale segmentation-oriented object target classification method achieves a classification accuracy of around 96%. This method improves classification accuracy by segmenting the RSI and aggregating pixel-level information into object-level information. However, the classification accuracy of

http://www.aloki.hu ● ISSN 1589 1623 (Print) ● ISSN 1785 0037 (Online)
DOI: http://dx.doi.org/10.15666/aeer/2305_92359253

this method is still limited because it only considers single-scale segmented objects and cannot fully capture the multi-scale features of different vegetation types in RSI. Conversely, deep learning and pixel-based target categorization methods achieve classification accuracies of approximately 92%. Measuring the changes of the five vegetation types in the Sanjiangyuan area, the results are shown in *Figure 13*.

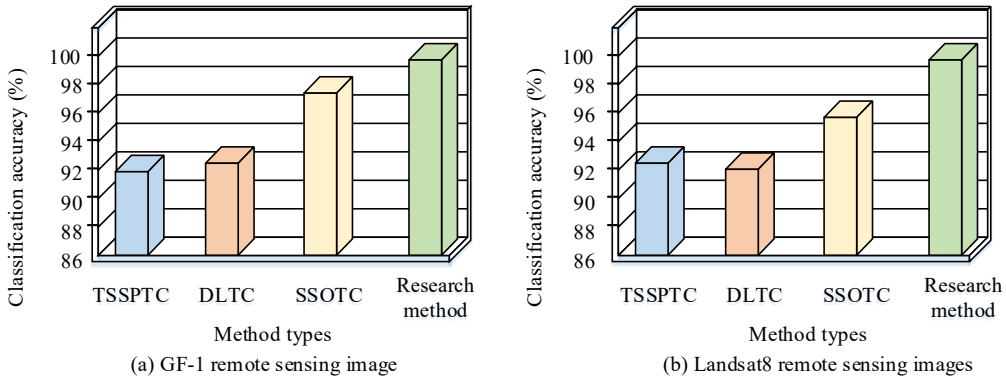

Figure 12. *Comparison of classification accuracy results of different classification methods*

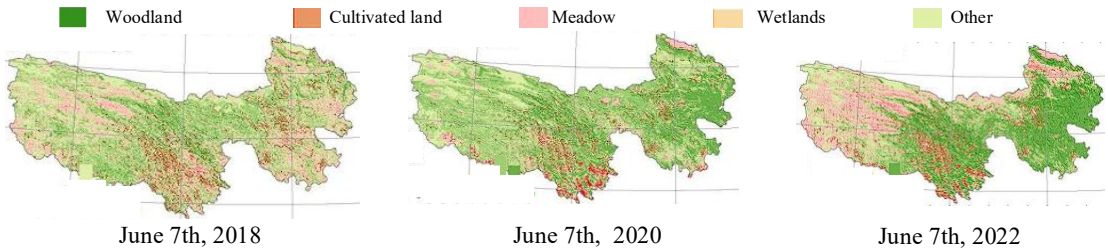

Figure 13. *Changes in the five vegetation types in the Sanjiangyuan area*

In *Figure 13*, the vegetation types in the Three Rivers Source Area are in DC. In June 7th, 2018, grassland and cropland occupy most of the area. In June 7th, 2020, both cropland and woodland increase, and grassland and wetland decrease. In June 7th, 2022, cropland and woodland further increase, with woodland mainly in the central and eastern parts, cropland mainly in the south, and grassland and other types of vegetation mainly in the northwestern part. In general, the DC of vegetation types in the Sanjiangyuan area will be affected by a variety of factors. Therefore, in order to support the area's sustainable development, it is essential to step up monitoring and study on the DC of various vegetation types in the Sanjiangyuan area as well as to design rational and scientific ecological protection measures. The changes in the proportion of vegetation types in the Sanjiangyuan area are shown in *Table 3*.

Table 3. *Changes in the proportion of vegetation types in the three rivers source area*

Year	Proportion of woodland (%)	Proportion of cultivated land (%)	Proportion of meadow (%)	Proportion of wetlands (%)	Proportion of other (%)
2018	8.2	**31.5**	**45.3**	9.6	5.4
2020	**12.7**(+4.5)	**34.8**(+3.3)	38.1(-7.2)	7.9(-1.7)	6.5(+1.1)
2022	**15.3**(+2.6)	**36.2**(+1.4)	32.5(-5.6)	6.1(-1.8)	9.9(+3.4)

http://www.aloki.hu ● ISSN 1589 1623 (Print) ● ISSN 1785 0037 (Online)
DOI: http://dx.doi.org/10.15666/aeer/2305_92359253

As shown in *Table 3,* cultivated and forest land continued to expand from 2018 to 2022, with net increases of 4.7% and 7.1%, respectively. This expansion is primarily driven by the cultivation of the southern river valley and the success of the reforestation project in the central and eastern mountainous regions. On the contrary, the proportion of grassland is sharply decreased by 12.8%, and the trend of desertification is evident in the high-altitude and cold regions of the northwest. The reduction of wetland area by 3.5% weakens the region's water conservation function. The increase of bare land, shrubs, and other types by 4.5% further exposes the region's ecological vulnerability.

Discussion and conclusion

The monitoring of VC in FE is a crucial initiative that can facilitate the long-term growth and stability of FE. Therefore, the study selected GF-1 and Landsat8 RSI as the primary RS information sources. Then, preprocessing operations such as radiometric correction, geometric correction, IF, and image mosaicing and cropping were performed on the RSI to improve its quality. Then the target area VC monitoring model was constructed based on the NDVCI threshold classification algorithm. The results revealed that in RSI preprocessing, the radiometric correction and geometric correction used in the study had better denoising effect. Its image gray mean distribution overlapped well with the OI gray mean curve, with an overlap of more than 99%. The IF method based on two-branch attention network adopted in the study maintained good consistency with the reference image in various indexes, and better restored the OI. The image mosaicing and cropping method adopted in the study could make the image clarity reach more than 90%. Through RSI preprocessing, the overall image quality could be substantially improved, providing a more reliable data base for subsequent studies. The NDVCI index threshold classification algorithm constructed in the study accurately demonstrated the VCov situation in the Sanjiangyuan area from 2018 to 2022. The hierarchical similarity region aggregation classification method used in the study had an accuracy of more than 98% for RSI vegetation type classification. In summary, the results adopted in the study can be used to assess the VC in the target area more accurately and comprehensively. However, the VC areas in different regions are distinguished by their multi-scale and irregular nature, which impairs the precision of the monitoring model. Consequently, subsequent studies will refine the monitoring method in accordance with the distinctive characteristics of different regions, thereby enhancing the accuracy of the model.

Declarations. All authors have read, understood, and have complied as applicable with the statement on "Ethical responsibilities of Authors" as found in the Instructions for Authors

Funding statement. There is no funding.

Competing interests. The authors disclose that they have no financial or non-financial interests.

REFERENCES

[1] Abba Haruna, A., Muhammad, L. J., Abubakar, M. (2022): Novel thermal-aware green scheduling in grid environment. – Artificial Intelligence and Applications 1(4): 244-251.

[2] Abd El-Ghany, N. M., Abd El-Aziz, S. E., Marei, S. S. (2020): A review: application of remote sensing as a promising strategy for insect pests and diseases management. – Environmental Science and Pollution Research 27(27): 33503-33515.

http://www.aloki.hu ● ISSN 1589 1623 (Print) ● ISSN 1785 0037 (Online)
DOI: http://dx.doi.org/10.15666/aeer/2305_92359253

[3] Al-Ali, Z. M., Abdullah, M. M., Asadalla, N. B., Gholoum, M. (2020): A comparative study of remote sensing classification methods for monitoring and assessing desert vegetation using a UAV-based multispectral sensor. – Environmental Monitoring and Assessment 192(6): 389-399.
[4] Al-Hamzawi, S. A. A., Awad, A. A., Salim, M. A. (2021): Using ArcGIS software and remote sensing technology to predict land surface temperature (LST) for monitoring ecological and climate change in Hor Al-Dalmaj, Southern Iraq. – IOP Conference Series Earth and Environmental Science 790(1): 12-16.
[5] Bhosle, K., Musande, V. (2023): Evaluation of deep learning CNN model for recognition of Devanagari digit. – Artificial Intelligence and Applications 1(2): 114-118.
[6] Chen, C., Wang, L., Zhang, Z., Lu, C., Chen, H., Chen, J. (2022): Construction and application of quality evaluation index system for remote-sensing image fusion. – Journal of Applied Remote Sensing 16(1): 1-15.
[7] Chenyu, Z., Shenliang, C., Peng, L. (2022): Spatiotemporal dynamic remote sensing monitoring of typical wetland vegetation in the Current Huanghe River Estuary Reserve. – Journal of Oceanography 44(1): 125-136.
[8] Chi, Z. (2021): Research on satellite remote sensing image fusion algorithm based on compression perception theory. – Journal of Computational Methods in Sciences and Engineering 21(2): 341-356.
[9] Cuaran, J., Leon, J. (2021): Crop monitoring using unmanned aerial vehicles: a review. – Agricultural Reviews 42(2): 121-132.
[10] Cui, X., Han, W., Zhang, H., Cui, J., Ma, W. T., Zhang, L., Li, G. (2023): Estimating soil salinity under sunflower cover in the Hetao Irrigation District based on unmanned aerial vehicle remote sensing. – Land Degradation and Development 34(1): 84-97.
[11] He, K. T., Li, Z. Z., Wang, D. M. (2022): Overview on the design of the service and management system for field geological survey based on the remote sensing and Beidou satellites. – Journal of Geomechanics 18(3): 203-212.
[12] Hu, R., Rao, B. S. M. R., Alaee-Kerahroodi, M., Ottersten, B. (2020): Orthorectified polar format algorithm for generalized spotlight SAR imaging with DEM. – IEEE Transactions on Geoscience and Remote Sensing 59(5): 1-9.
[13] Huang, M., Liu, S., Li, Z., Feng, S., Shu, F. (2022): Remote sensing image fusion algorithm based on two-stream fusion network and residual channel attention mechanism. – Wireless Communications and Mobile Computing 22(6): 1590-1598.
[14] Hussain, S., Karuppannan, S. (2023): Land use/land cover changes and their impact on land surface temperature using remote sensing technique in district Khanewal, Punjab Pakistan. – Geology, Ecology, and Landscapes 7(1): 46-58.
[15] Jiang, R., Liu, J. (2024): Characterization and projection of spatial and temporal changes in habitat quality of Sanjiangyuan based on land use change. – Journal of Geographical Sciences 34(9): 1797-1821.
[16] Kattenborn, T., Leitloff, J., Schiefer, F., Hinz, S. (2021): Review on Convolutional Neural Networks (CNN) in vegetation remote sensing. – ISPRS Journal of Photogrammetry and Remote Sensing 173(5): 24-49.
[17] Lawrance, N. A., Angel, T. S. S. (2023): Image fusion based on NSCT and sparse representation for remote sensing data. – Computer Systems Science and Engineering 46(9): 3439-3455.
[18] Li, Y. (2021): Interpretation of the status quo of domestic ecological environment quality based on remote sensing technology. – IOP Conference Series Earth and Environmental Science 692(4): 42-48.
[19] Liu, J., Jia, R., Li, W., Ma, F., Wang, X. (2020): Image dehazing method of transmission line for unmanned aerial vehicle inspection based on densely connection pyramid network. – Wireless Communications and Mobile Computing 20(4): 1-9.

http://www.aloki.hu ● ISSN 1589 1623 (Print) ● ISSN 1785 0037 (Online)
DOI: http://dx.doi.org/10.15666/aeer/2305_92359253

[20] Min, L., Wang, N., Wu, L., Li, N., Zhao, J. (2020): Inversion of Yellow River runoff based on multi-source radar remote sensing technology. – Dianzi Yu Xinxi Xuebao/Journal of Electronics and Information Technology 42(7): 1590-1598.
[21] Pan, Y., Pi, D., Chen, J., Chen, Y. (2021): Remote sensing image fusion with multistream deep ResCNN. – Journal of Applied Remote Sensing 15(3): 1-19.
[22] Paz-Alberto, A. M., Camaso, E., Alberto, R. P., Juganas, D. A., Mapanao, K. M., Ponce, C. D. B. (2021): Climate change vulnerability and disaster risk assessment using remote sensing technology and adaptation strategies for resiliency and disaster risk management in selected coastal municipalities of Zambales, Philippines. – American Journal of Climate Change10(1): 85-133.
[23] Virnodkar, S. S., Pachghare, V. K., Patil, V. C., Jha, S. K. (2020): Remote sensing and machine learning for crop water stress determination in various crops: a critical review. – Precision Agriculture 21(5): 1121-1155.
[24] Xie, Y., Han, X., Zhu, S. (2021): Synthesis of true color images from the Fengyun advanced geostationary radiation imager. – Journal of Meteorological Research 35(6): 11136-1147.
[25] Xu, S., Amira, O., Liu, J., Zhang, C. X., Zhang, J., Li, G. (2020): HAM-MFN: hyperspectral and multispectral image multiscale fusion network with RAP loss. – IEEE Transactions on Geoscience and Remote Sensing 58(7): 4618-4628.
[26] Xue, W., Zhang, Z., Chen, S. (2021): Ghost elimination via multi-component collaboration for unmanned aerial vehicle remote sensing image stitching. – Remote Sensing 13(7): 1388-1392.
[27] Yang, Y., Lu, H., Huang, S., Tu, W. (2020): Remote sensing image fusion based on fuzzy logic and salience measure. – IEEE Geoscience and Remote Sensing Letters 17(11): 1943-1947.
[28] Zeng, Y., Hao, D., Huete, A., Dechant, B., Berry, J., Chen, J. M., Chen, M. (2021): Optical vegetation indices for monitoring terrestrial ecosystems globally. – Nature Reviews Earth & Environment 3(7): 477-493.
[29] Zhang, C., Chen, Y., Yang, X., Gao, S., Sun, L. (2020): Improved remote sensing image classification based on multi-scale feature fusion. – Remote Sensing 12(2): 213-219.
[30] Zhang, Y., Shao, Z. (2021): Assessing of urban vegetation biomass in combination with LiDAR and high-resolution remote sensing images. – International Journal of Remote Sensing 42(3): 964-985.
[31] Zhang, Y., Yao, X., Zhou, S., Zhang, D. (2022): Glacier changes in the Sanjiangyuan Nature Reserve of China during 2000-2018. – The geographical journal 32(2): 259-279.
[32] Zhong, L., Liu, X. S., Yang, P., Lin, R. Z. (2020): Explore the application of high-resolution nighttime light remote sensing images in nighttime marine ship detection: a case study of LJ1-01 data. – Open Geosciences 12(1): 1169-1184.

http://www.aloki.hu ● ISSN 1589 1623 (Print) ● ISSN 1785 0037 (Online)
DOI: http://dx.doi.org/10.15666/aeer/2305_92359253